applied optics

# Wafer defect detection by a polarization-insensitive external differential interference contrast module

Amit Nativ,[1] Haim Feldman,[2] and Natan T. Shaked[1,*]

[1]Department of Biomedical Engineering, Faculty of Engineering, Tel Aviv University, Tel Aviv 69978, Israel
[2]Applied Materials Israel, Rehovot 76705, Israel
*Corresponding author: nshaked@tau.ac.il

Received 18 January 2018; revised 18 March 2018; accepted 21 March 2018; posted 21 March 2018 (Doc. ID 319722); published 27 April 2018

**We present a system that is based on a new external, polarization-insensitive differential interference contrast (DIC) module specifically adapted for detecting defects in semiconductor wafers. We obtained defect signal enhancement relative to the surrounding wafer pattern when compared with bright-field imaging. The new DIC module proposed is based on a shearing interferometer that connects externally at the output port of an optical microscope and enables imaging thin samples, such as wafer defects. This module does not require polarization optics (such as Wollaston or Nomarski prisms) and is insensitive to polarization, unlike traditional DIC techniques. In addition, it provides full control of the DIC shear and orientation, which allows obtaining a differential phase image directly on the camera (with no further digital processing) while enhancing defect detection capabilities, even if the size of the defect is smaller than the resolution limit. Our technique has the potential of future integration into semiconductor production lines.** 

***OCIS codes:*** (120.3930) Metrological instrumentation; (120.4290) Nondestructive testing; (120.5050) Phase measurement; (180.3170) Interference microscopy.

https://doi.org/10.1364/AO.57.003534

## 1. INTRODUCTION

Detecting defects in semiconductor wafers is a crucial step during the wafer manufacturing process, since defects escaping detection have significant financial meaning. In contrast to using scanning electron microscopy (SEM) or atomic force microscopy (AFM) as wafer defect inspection tools, optical imaging tools are faster, simpler, and less expensive. Thus, although providing lower-resolution capabilities, optical imaging tools are preferred as a first step of detecting "hot spots" of defects before sending selected wafers to SEM or AFM. Critical dimensions of semiconductor wafer architectures continue to reduce far below the optical resolution limit, and so do the manufacturing defects [1], making defect detection challenging for optical inspection tools. While increasing the optical resolution is one approach, the actual limiting factor for defect detection is the optical system noise [2]. Thus, detection sensitivity improves if the noise level in the system reduces.

Many defect inspection tools rely on the wafer periodic pattern and subtract between seemingly similar areas on the wafer along the defect inspection pipeline. The subtraction image enhances irregularities in the wafer pattern, and, if any defect is present, it will be revealed in the subtraction image, given the defect signal is stronger than the noise of the subtracted periodic pattern [3–8]. It is therefore important to enhance the defect signal over the pattern signal, as early as possible, hopefully during the image acquisition stage of the inspected area.

Optical detectors such as digital cameras are sensitive to optical intensity but are insensitive to optical phase changes. Such phase changes originate from the slight delay of light interacting with the sample. This light delay is directly proportional to spatial changes in the sample thickness, sample refractive index, or both. When imaging wafers, the phase distribution of an optical wave reflecting from the wafer indicates its surface topography. Irregularities in the wafer topography indicate defects in the wafer fabrication process [3,4,9–11] and can damage the final semiconductor device. Without imaging phase variations, vital information about the wafer pattern is lost.

Differential interference contrast (DIC) microscopy [12,13] uses light interference to view optical phase variations across the sample. In a typical DIC microscope, a linearly polarized beam is split into two orthogonally polarized, mutually coherent, and laterally shifted beams using a Nomarski or a Wollaston prism [14]. The two orthogonally polarized beams illuminate the sample with a lateral shear between them, which is typically smaller than the optical diffraction limit. After interacting with the sample, another identical prism and a polarizer are used to combine the beams and to align their polarizations. The result is an interference image, which represents the spatial phase gradient along the direction of the shear [15].

Over the years, different DIC setups have been developed, such as Köhler-DIC and Plas-DIC [16]. However, these setups require accurate calibration, and part of them relies on polarized light, using a polarizing prism to split and/or combine the beams before and after the sample, making it difficult to image birefringent samples. Although DIC setups relying on polarizing prisms have become the most popular, DIC imaging can also be achieved by shearing interferometers, connected after the imaging plane of a microscope. In such setups, the microscope output beam is split, and then the two beams are superimposed on the detector with a lateral shear [17–24]. The disadvantage of splitting the beam after illuminating the sample is the limit on the shear length, which must be inside the coherence radius of illumination. The benefits of these systems are their simplicity and insensitivity to polarizing samples because the beam splitting, shearing, and combining occur after the light interacts with the sample without using any polarizing prisms.

In this paper, we propose an external DIC module specifically adapted for optically detecting wafer defects. In order to enhance the defect signal, we slightly shear one beam relative to the other one; this creates a differential image, where the defect signal is increased relative to the surrounding pattern. This DIC module is composed of a robust shearing interferometric module, which connects externally at the output of a microscope and enables easy control of the shear direction and size. Like other shearing interferometers, it has a limitation on the shear length between the externally sheared beams, but, as the critical dimensions of the wafer architecture become smaller, this limiting condition is relaxed, and less coherent light may be used. We compare the signal-to-noise ratio (SNR) of defects taken under bright-field (BF) imaging and by our DIC module under the same environmental and illumination conditions. Using our DIC module, we were able to increase the SNR of defects as small as 150 nm without any post-processing, while our optical resolution limit was 590 nm.

## 2. OPTICAL SETUP

The optical setup is shown Fig. 1. A reflection microscope with 0.95 NA, 50× objective lens (MO) [Olympus MPLAPON50x followed by a tube lens (TL, $f = 180$ mm)] was supplemented with an additional 4f lens configuration [lenses L5 ($f = 75$ mm) and L6 ($f = 100$ mm)] for total magnification of 60×. The microscope is illuminated by a spatial-coherence-controlled source, made out of a coherent DPSS laser source (532 nm, 96.1 mW, Laser Glow Technologies), followed by a rotating diffuser (Thorlabs N-BK7 ground glass, 1500 grit, mounted on 2342S 012CR FAULHABER DC engine) and a spatial filter [lenses L1 ($f = 25.4$ mm), L2 ($f = 50$ mm) and pinhole P1 (400 μm)]. Lenses L3 ($f = 100$ mm) and L4 ($f = 250$ mm) are used to image pinhole P1 on the back focal plane of the objective, creating a Köhler illumination configuration, with an effective condenser numerical aperture of NA = 0.15 [25,26].

The DIC module is a specially designed shearing interferometer that allows full control on the shearing distance and angles. The module is connected at the microscope output image plane. Mirrors M1 and M2 are located at the Fourier plane at the middle of a 4f lens system [lenses L7 ($f = 100$ mm), L8 ($f = 180$ mm)], and beam splitter BS2 splits the microscope output beam into two beams. To align mirrors M1 and M2, standard manual mechanical stages are used. Due to the Fourier plane relation between the mirrors and the image plane, by tilting mirror M1 relative to M2, the two beams are shifted relative to each other but remain parallel on the image plane, creating the required shearing for the DIC image on the camera. Because the beam shearing is practically performed after the microscope image plane, the shearing length and orientation are easily adjusted. If the shift between the beams is within the spatial coherence radius of the illumination, the beams will interfere, and a differential image will be recorded on the camera. Lenses L9 ($f = -30$ mm) and L10 ($f = 60$ mm) compose a 4f lens configuration for additional magnification, which relaxes effects of mechanical misalignments of mirrors M1 and M2 relative to the Fourier plane of lens L7. The total magnification of the sample on the camera is 240×, and the total field of view is 27 μm × 22 μm, which is suitable for wafer contacts of up to a few micrometers in size. Our optical resolution limit was 590 nm. Because the system is intended for detecting and localizing defects and not for fully imaging them, possible effects of relay lens aberrations are negligible.

To control the DIC bias between the beams, a variable wave retarder (VWR) plate (Thorlabs LCC1115-A) is placed in front of mirror M2. To ensure the VWR acts as a wave retarder rather than changes the circularity of the polarization, a polarizer is

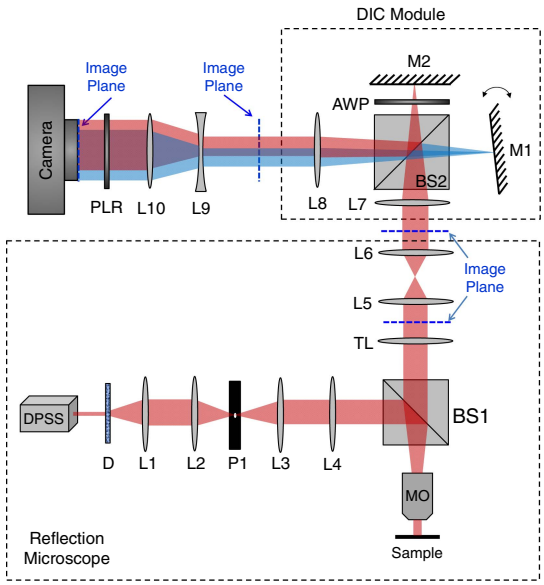


**Fig. 1.** Optical setup for wafer defect inspection containing a spatial-coherence-controlled external DIC module. D, rotating diffuser. L1, L2, lenses composing a 4f system to image the diffused light on pinhole P1, used to control the amount of spatial coherence illuminating the microscope. L3, L4, lenses composing a 4f system to image the pinhole on the back focal plane of the objective MO. TL, tube lens. L5, L6, lenses composing a 4f system for additional magnification. The DIC module includes: L7 and L8, lenses composing a 4f system; BS2, beam splitter; M1, M2, mirrors located at the Fourier plane of L3; VWR, variable wave retarder plate, used to create the DIC bias; L9, L10, lenses creating an additional magnification; and PLR, linear polarizer.

placed before the camera. To calibrate the VWR axis, first the beam reflecting from M2 is blocked. Then, the polarizer is rotated until the maximum intensity on the camera is reached. Next, the beam reflecting from M1 is blocked, and the VWR is rotated until the intensity on the camera remains the same even if the supply voltage of the VWR changes. Note that the polarizer and the VWR are used merely to control the DIC bias and can be removed if bias control is not needed. In contrast with traditional DIC methods, the light entering the proposed DIC module does not need to be polarized first.

Note that in spite of using partial spatially incoherent illumination, the light source was temporally coherent; thus, the relative distance between the mirrors can be straightforwardly adjusted even manually, yielding interference in a rather simple way.

## 3. THEORETICAL MODEL OF DIC MODULE

A DIC image is formed from the interference of two images of the sample, which are laterally sheared but overlap on the camera. To improve image quality, a relative bias between images is induced by adding a constant phase delay between the two beams.

In our system, the DIC shear is created after the image plane as a result of the different tilts of mirrors M1 and M2, and the constant phase delay creating the bias is caused by the VWR. As a consequence, each pixel represents the subtraction of different regions on the sample, where the typical DIC theoretical model described in [16] still holds. We shortly describe this model here for completeness.

The output beam of the microscope is split in two by beam splitter BS2 and Fourier transformed by lens L7. A relative tilt between mirrors M1 and M2 in the Fourier plane of L7 creates a spatial shear between the two beams in the image plane at the exit of the DIC module. Assuming equal reflections from mirrors M1 and M2, the PSF of the DIC optical imaging system for fully coherent illumination is given by

$$h^c_{\mathrm{DIC}}(x,y) = h^c(x+\Delta,y)\exp(-j\phi) - h^c(x-\Delta,y)\exp(j\phi), \tag{1}$$

where $h^c_{\mathrm{DIC}}$ is the DIC point spread function (PSF) under fully coherent illumination, $h^c$ is the coherent PSF under fully spatially coherent illumination, $2\Delta$ is the relative shear between the two beams exiting the DIC module at the image plane, and $2\phi$ is the constant phase introduced by the VWR in a round trip. Equation (1) shows that the contrast mechanism in DIC is the gradient of the sample phase in the direction of the shear.

The coherent transfer function (CTF) is given by

$$P^c_{\mathrm{DIC}}(\xi,\eta) = P^c(\xi,\eta)\exp[j(2\pi\xi\Delta-\phi)] - P^c(\xi,\eta)\exp[-j(2\pi\xi\Delta-\phi)], \tag{2}$$

where $P^c$ is the coherent transfer function of the BF microscope, and $\xi$, $\eta$ are transverse coordinates in the objective back focal plane. In the case of an ideal aberration-free BF system, $P^c$ is a circle with radius equal to the numerical aperture NA of the objective divided by the illumination wavelength $\lambda$. This model is true only when the illumination is fully coherent.

To improve our system image quality and SNR, we illuminate the microscope by a spatially and temporally coherent DPSS laser source passing through a rotating diffuser. The rotating diffuser destroys the spatial coherence of the source. Because no interference of sheared beams can be achieved under fully spatially incoherent illumination, we filter the spatially incoherent light after the diffuser through pinhole P1, and increase the spatial degree of coherence so that the beams can interfere on the camera.

For partial coherence illumination, the partially coherent transfer function is given by

$$C_{\mathrm{DIC}}(m,n;p,q) = \int_{-\infty}^{\infty}\int_{-\infty}^{\infty}|P_{\mathrm{cond}}(\xi,\eta)|^2 P^c_{\mathrm{DIC}}(\xi-m,\eta-n) \times P^{c*}_{\mathrm{DIC}}(\xi-p,\eta-q)\mathrm{d}\xi\mathrm{d}\eta, \tag{3}$$

where $P_{\mathrm{cond}}$ is the coherent transfer function of the condenser, which in our system equals to the coherent transfer function of the objective lens, limited by the image of pinhole P1 on its back focal plane, and $(m;p)$, $(n;q)$ are the normalized spatial frequency pairs in $x$ and $y$ directions, as defined in [16]. In the case of an ideal aberration-free system, Eq. (3) has a simple geometric meaning of three overlapping circles. Because the camera detects only the intensity, the image on the camera under partially coherent illumination is given as follows:

$$I_{\mathrm{DIC}}(x,y) = \int_{-\infty}^{\infty}\int_{-\infty}^{\infty}\int_{-\infty}^{\infty}\int_{-\infty}^{\infty} T(m,n)T^*(p,q)C_{\mathrm{DIC}}(m,n;p,q) \times \exp\{2\pi j[(m-p)x+(n-q)y]\}\mathrm{d}m\mathrm{d}n\mathrm{d}p\mathrm{d}q, \tag{4}$$

where $T(m,n)$ is the sample spatial spectrum.

## 4. RESULTS

To experimentally demonstrate the defect enhancement capabilities of the proposed DIC module, we used a silicon wafer test target, having programmed bridge defects of various sizes in known locations (courtesy of Applied Material Israel). The wafer pattern is constructed of short silicon features of 3 μm × 0.4 μm × 0.150 μm with 3.6 μm pitch on one axis and 6 μm pitch on the second axis. The short silicon features are surrounded by long lines (0.4 μm width × 0.150 μm height), as shown in Fig. 2.

We used the proposed DIC module to enhance the bridge defect signal over the pattern signal by introducing small shears by manually tilting mirror M1. The bridge defects are all 0.5 μm in length but change in width: 0.5 μm, 0.4 μm, 0.35 μm, 0.275 μm, 0.2 μm, and 0.15 μm. Using our module,

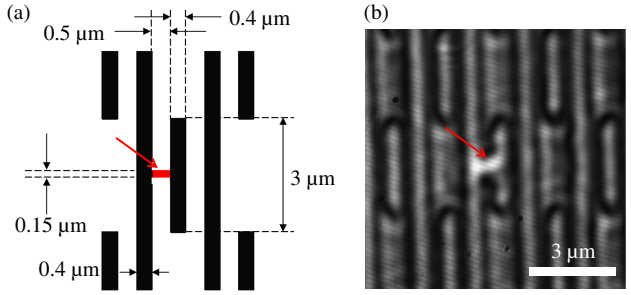


**Fig. 2.** Test wafer pattern. (a) Scheme of the wafer imaged, with its dimensions written and the bridge defect indicated by a red arrow. (b) Image taken under fully spatially incoherent illumination (obtained by removing pinhole P1).

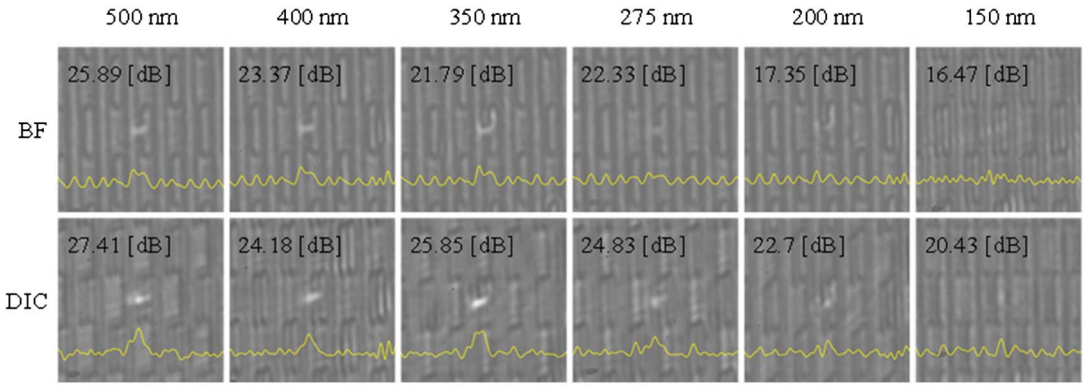


**Fig. 3.** Bridge defects in scales varying from 500 to 150 nm in width and length of 500 nm. For each scale, the BF and the DIC images were acquired under the same illumination conditions and same position. DIC images were acquired by shearing the beams in the direction parallel to the bridge defect orientation using the proposed external DIC module. Images are normalized. As can be seen, our method obtained improvement in the defect PSNR for all defect scales.

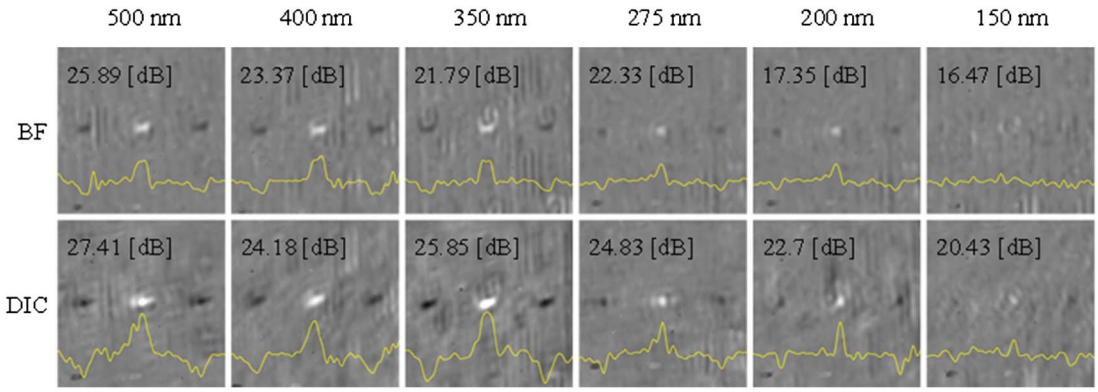


**Fig. 4.** Second-order difference images of bridge defects for the coinciding cases of Fig. 3.

we could fully control the shearing size and orientation. Therefore, the shift size and direction were adjusted for every scale to produce the highest intensity from the defect relative to the surrounding pattern.

To measure the quality of the results, first we normalized each image by subtracting its mean and dividing it by its standard deviation. This was done in order to decrease influences of different illumination intensities or camera exposure times. We then measured the intensity of the defect relative to the pattern by using peak signal-to-noise ratio (PSNR), defined as follows:

$$\mathrm{PSNR} = 20\log_{10}(D_{\mathrm{defect}}/\sigma), \tag{5}$$

where $D_{\mathrm{defect}}$ is the peak intensity of the defect image, and $\sigma$ is the standard deviation of the whole image (which is unity in the normalized image). Figure 3 shows the normalized image of each scale, along with the cross section of the defect in the horizontal direction. For each image, the PSNR value was calculated, as indicated on the figure, demonstrating the increased PSNR obtained.

To further enhance the PSNR by averaging spatial noise, we calculated the PSNR of the second-order difference of the defect. This is done by digitally subtracting between three images of areas that are spaced one period of the pattern away from each other [3]. The subtraction image is calculated as follows:

$$I(x,y) = -I_{-1}(x,y) + 2I_0(x,y) - I_{+1}(x,y), \tag{6}$$

where $I_{-1}$ is taken one period of the pattern (3.6 μm) to the left of the defect, and $I_{+1}$ is taken one period of the pattern to the right of the defect. $I_0$ is acquired with the defect at the center of the image. As can be seen, indeed the effect of second-order

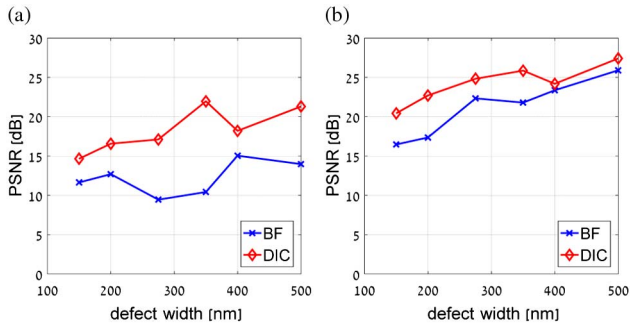


**Fig. 5.** Defect PSNR using BF imaging and using the proposed DIC module. (a) PSNR values obtained for images without post-processing (as measured directly on the camera). (b) PSNR values obtained after digitally post-processing the images by second-order differencing. Our DIC module increases defect PSNR in every scale in both methods.

difference of areas located one pattern period apart is averaging spatial noise, thus increasing the SNR of the defect. We calculated the PSNR according to Eq. (5), but in this case the standard deviation calculation excluded the area in the proximity of the defect, to avoid the negative values around it, caused by the image subtraction, which increases the standard deviation. Figure 4 shows the second-order difference images for the same defects shown in Fig. 3. As can be seen, the PSNR for both BF and DIC images improves due to the averaging of spatial noise, but still DIC yields a higher PSNR for every scale in comparison to BF.

We summarize our results of the PSNR of the DIC images for various defect widths in Fig. 5. As can be seen from these graphs, our method increased the defect signal over the pattern with and without second-order difference image.

## 5. CONCLUSION

In this paper, we proposed a new method for optically enhancing detection of semiconductor defects over their surrounding pattern, by using a compact, external module that can turn an existing microscope illuminated with temporally coherent and partially spatially coherent light to a DIC microscope. Our DIC module is insensitive to polarization; thus, it is not using polarizing prisms, as in regular DIC microscopy, and the DIC image is created externally to the imaging system. By adjusting the DIC shear and orientation, we increased the optical signal of the defects relative to the optical signal of their surrounding pattern. This makes our system beneficial, especially for patterned wafers because, in contrast with other imaging systems, such as dark-field microscopy, which cannot directly distinguish between an edge of a defect and an edge of a contact, our system does not require any post-processing to suppress the optical signal of the surrounding wafer pattern and reveals the defects directly on the camera. Despite the fact that we were not able to directly image defects smaller than the resolution limit, we were able to localize them using the system. In order to obtain a full wafer scan, automatic sample scanning and larger sensor sizes should be used. Full wafer scanning automation will also require automatic focusing. We believe that this module will be suitable for external integration into various wafer inspection machines that have a BF microscopy path inside.

**Funding.** XIN Center at Tel Aviv University; Israeli Ministry of Economy and Applied Materials Israel (NOFAR).

## REFERENCES

1. T. F. Crimmins, "Defect metrology challenges at the 11-nm node and beyond," Proc. SPIE **7638**, 76380H (2009).
2. T. F. Crimmins, "Wafer noise models for defect inspection," Proc. SPIE **7971**, 79710E (2011).
3. R. Zhou, C. Edwards, A. Arbabi, G. Popescu, and L. L. Goddard, "Detecting 20 nm wide defects in large area nanopatterns using optical interferometric microscopy," Nano Lett. **13**, 3716–3721 (2013).
4. R. Zhou, C. Edwards, C. A. Bryniarski, G. Popescu, and L. L. Goddard, "9 nm node wafer defect inspection using three-dimensional scanning, a 405 nm diode laser, and a broadband source," Proc. SPIE **9424**, 942416 (2015).
5. R. Zhou, G. Popescu, and L. L. Goddard, "22 nm node wafer inspection using diffraction phase microscopy and image post-processing," Proc. SPIE **8681**, 86810G (2013).
6. T. S. Newman and A. K. Jain, "A survey of automated visual inspection," Comput. Vis. Image Underst. **61**, 231–262 (1995).
7. N. G. Shankar and Z. W. Zhong, "Defect detection on semiconductor wafer surfaces," Microelectron. Eng. **77**, 337–346 (2005).
8. M. Zontak, I. Cohen, M. Zontak, and I. Cohen, "Defect detection in patterned wafers using anisotropic kernels," Mach. Vis. Appl. **21**, 129–141 (2010).
9. T. Terasawa, T. Amano, T. Yamane, H. Watanabe, M. Toyoda, T. Harada, T. Watanabe, and H. Kinoshita, "At wavelength observation of phase defect embedded in EUV mask using microscope technique," Proc. SPIE **9048**, 904825 (2014).
10. Y.-G. Wang, R. Miyakawa, W. Chao, K. Goldberg, A. Neureuther, and P. Naulleau, "Phase-enhanced defect sensitivity for EUV mask inspection," Proc. SPIE **9235**, 92350L (2014).
11. H. Yue, Y. Wu, B. Zhao, Z. Ou, and Y. Liu, "High-accuracy inspection of defects and profile of wafers by phase measuring deflectometry," Proc. SPIE **9282**, 928208 (2014).
12. F. H. Smith, "Interference microscope," U.S. patent 2,601,175 A (5 August 1947).
13. G. Nomarski, "Interferential polarizing device for study of phase objects," U.S. patent 2,924,142 (14 May 1952).
14. R. D. Allen, G. B. David, and G. Nomarski, "The Zeiss-Nomarski differential interference equipment for transmitted-light microscopy," Z. Wiss. Mikrosk. **69**, 193–221 (1969).
15. C. Preza, D. L. Snyder, and J.-A. Conchello, "Theoretical development and experimental evaluation of imaging models for differential-interference-contrast microscopy," J. Opt. Soc. Am. A **16**, 2185–2199 (1999).
16. S. B. Mehta and C. J. R. Sheppard, "Partially coherent image formation in differential interference contrast (DIC) microscope," Opt. Express **16**, 19462–19479 (2008).
17. X. Cui, M. Lew, and C. Yang, "Quantitative differential interference contrast microscopy based on structured-aperture interference," Appl. Phys. Lett. **93**, 091113 (2008).
18. T. J. McIntyre, C. Maurer, S. Bernet, and M. Ritsch-Marte, "Differential interference contrast imaging using a spatial light modulator," Opt. Lett. **34**, 2988–2990 (2009).
19. T. J. McIntyre, C. Maurer, S. Fassl, S. Khan, S. Bernet, and M. Ritsch-Marte, "Quantitative SLM-based differential interference contrast imaging," Opt. Express **18**, 14063–14078 (2010).
20. G. Pretzler, H. Jager, and T. Neger, "High-accuracy differential interferometry for the investigation of phase objects," Meas. Sci. Technol. **4**, 649–658 (1993).
21. F. Zastavnik, L. Pyl, J. Gu, H. Sol, M. Kersemans, and W. V. Paepegem, "Calibration and correction procedure for quantitative out-of-plane shearography," Meas. Sci. Technol. **26**, 045201 (2015).
22. M. Pluta, *Advanced Light Microscopy* (Elsevier, 1989), Vol. **2**.
23. H. Schreiber and J. Schwider, "Lateral shearing interferometer based on two Ronchi phase gratings in series," Appl. Opt. **36**, 5321–5324 (1997).
24. L. Chen, X. Liu, and Y. Gao, "A novel lateral shearing interferometer and its anti-vibration characteristic for on-machine precision surface measurement," Optik **127**, 5729–5737 (2016).
25. A. Nativ and N. T. Shaked, "Compact interferometric module for full-field interferometric phase microscopy with low spatial coherence illumination," Opt. Lett. **42**, 1492–1497 (2017).
26. C. Edwards, B. Bhaduri, T. Nguyen, B. G. Griffin, H. Pham, T. Kim, G. Popescu, and L. L. Goddard, "Effects of spatial coherence in diffraction phase microscopy," Opt. Express **22**, 5133–5146 (2014).